photonics

MDPI

Article

Simulation Analysis of Mode Hopping Impacts on OFDR Sensing Performance

Qirui Wang [1], Nageswara Lalam [2], Kehao Zhao [1], Shuda Zhong [1], Guangyin Zhang [1], Ruishu Wright [2] and Kevin P. Chen [1,*]

[1] Department of Electrical and Computer Engineering, University of Pittsburgh, Pittsburgh, PA 15261, USA; qiw53@pitt.edu (Q.W.); kez23@pitt.edu (K.Z.); shz116@pitt.edu (S.Z.); guz33@pitt.edu (G.Z.)
[2] National Energy Technology Laboratory, Pittsburgh, PA 15236, USA; nageswara.lalam@netl.doe.gov (N.L.); ruishu.wright@netl.doe.gov (R.W.)
* Correspondence: pec9@pitt.edu

Abstract: This article examines the impacts of mode hopping on the sensing performance of optical frequency domain reflectometry (OFDR) and explores the potential for developing economical OFDR interrogators employing low-cost distributed feedback (DFB) lasers. By conducting numerical simulations, this study reveals that mode hopping has minimal effects on distance sensing measurements in free space due to the limited duration of beat interference signal at the incorrect frequency within the coherence length. Additionally, the simulations indicate that mode hopping only slightly affects the distributed strain sensing of OFDR, resulting in an error range of less than ±1 με when 100 με is applied to the sensing fiber. These findings highlight the potential of using low-cost DFB lasers with a 1-nm wavelength sweep range and a 1-MHz linewidth as tunable laser sources in OFDR while maintaining reliable and accurate sensing performance.

Keywords: distributed feedback laser; LiDAR; mode hopping; optical frequency domain reflectometry

check for updates

Citation: Wang, Q.; Lalam, N.; Zhao, K.; Zhong, S.; Zhang, G.; Wright, R.; Chen, K.P. Simulation Analysis of Mode Hopping Impacts on OFDR Sensing Performance. *Photonics* **2024**, *11*, 580. https://doi.org/10.3390/photonics11060580

Received: 20 May 2024
Revised: 13 June 2024
Accepted: 19 June 2024
Published: 20 June 2024

Correction Statement: This article has been republished with a minor change. The change does not affect the scientific content of the article and further details are available within the backmatter of the website version of this article.

1. Introduction

Optical frequency domain reflectometry (OFDR) is a coherent homodyne technique wherein Rayleigh backscattered light is combined with reference light to extract the strain or temperature information along the fiber length. It can achieve fully distributed sensing performance with exceptional spatial resolution, enhanced sensitivity, and a large dynamic range, thus attracting considerable interest in recent years. By utilizing a swept-wavelength continuous wave interferometry configuration, OFDR can overcome the limitations of conventional optical time domain interferometry and enable the detection and characterization of micro-scale changes in the sensing fiber. OFDR has found numerous applications in various industries, including aerospace, oil and gas, telecommunications, and civil engineering, as well as distance measurements in free-space or light detection and ranging (LiDAR) applications [1–7].

A critical component within the OFDR system is the tunable laser source. To achieve highly reliable OFDR measurements over extended interrogation lengths, the tunable laser must possess both a long coherence length and the capacity for stable sweep linearity and mode-hopping-free wavelength tuning. External cavity-tuned diode lasers are commonly employed in OFDR applications due to their wider wavelength tuning range, stability, and narrow linewidth characteristics [8]. However, these lasers are costly, contributing significantly to the overall expenditure of the OFDR system.

Recent advancements in semiconductor optoelectronic technology have led to substantial improvements in the optical performance of distributed feedback (DFB) diode lasers, particularly regarding optical coherence and output power [9–11]. Commercial off-the-shelf DFB lasers with an emission wavelength of around 1550 nm can attain spectral widths as narrow as 100 kHz. This narrow width potentially allows for the interrogation of sensing fibers up to a length of

1 km. Furthermore, through current tunning, the wavelength of DFB diode lasers can be swiftly modulated over a span of 1 nm. Theoretically, this capability facilitates achieving an 800-µm spatial resolution [12]. Another significant advantage of current-tuned DFB lasers lies in their potential for rapid interrogation through direct current modulation, which is much faster than using external mechanical or piezo-electric tuned optical components.

However, the issue of mode hopping remains a widely held concern for current-tuned DFB lasers. Generally, DFB lasers maintain a stable mode without mode hopping under normal operational conditions. Nevertheless, they can exhibit mode hopping due to thermal effects, mechanical stress, current instabilities, and aging, which are common for field or outdoor measurements. These factors can affect the grating period, refractive index, or gain profile within the laser cavity, potentially causing the output wavelength to “hop” by up to sub-nanometer scales [13–15]. Such abrupt shifts in wavelength or optical frequency are generally deemed unsuitable for distributed fiber sensing or LiDAR applications. As a result, most research and development efforts to advance high-performance tunable diode lasers have been directed toward mitigating mode hopping issues and ensuring stable, single-frequency operation [16–18].

In this study, the mode hopping issue is explored from an alternative perspective. While there is a prevailing consensus in the optical science community that mode hopping presents a major hindrance to high-performance sensing applications, this research probes the degree of performance deterioration in OFDR-based optical sensing when utilizing a laser prone to mode hopping. Through theoretical analysis and numerical simulations, this article will shed light on the notion that the sensing performance of OFDR systems would not be severely compromised, and acceptable performance can be maintained with the presence of mode hopping in low-cost DFB lasers. This understanding would mean substantial potential to significantly reduce the financial burden associated with OFDR systems and enable more widespread deployment.

2. OFDR LiDAR Distance Sensing Simulations

One common application of OFDR is in measuring distances to the surface of a device under test (DUT). An example of a free-space OFDR LiDAR distance sensing system in practice is shown in Figure 1. A low-cost DFB tunable laser (TL, Furukawa Fitel FRL15DCWD) with a 1-nm wavelength sweep range is used as the optical source, and its linewidth is 1 MHz. The output of the TL is split into two arms using a 90/10 optical coupler. The low-power arm is linked to an auxiliary Mach–Zehnder interferometer with a 5-m fiber length disparity, which serves to compensate for the nonlinear frequency tuning of the TL. Concurrently, the high-power arm is fed into two polarization controllers (PCs) that make up the main interferometer, along with an attenuator (AT) and a collimator (COLL). When the laser light emitted from the collimator is reflected off the DUT and returns through the circulator, it interferes with the reference arm’s light at the 50/50 optical coupler. Two photodetectors (PDs) and a data acquisition (DAQ) device are used to acquire interference signals from both interferometers. The distance between the collimator and the DUT is proportional to the beat frequency of the main interferometer’s interference signal.

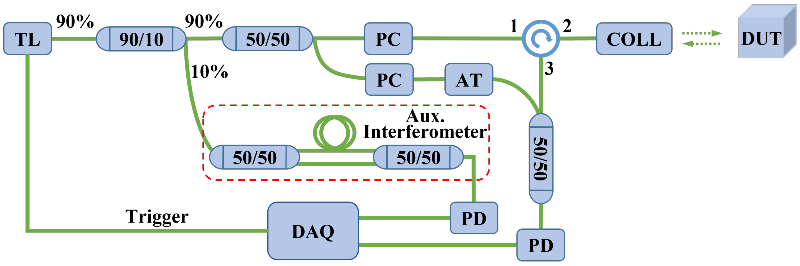

Figure 1. Schematic of a free-space OFDR LiDAR distance sensing system.

The simulations were conducted employing parameters analogous to those used in the practical OFDR sensing system. However, to specifically address the issue of mode hopping, nonlinear optical frequency tuning was excluded from the simulation, and each optical frequency sweep of the TL was a linear process [19]. Table 1 provides a summary of the foundational parameters utilized in the OFDR sensing simulations. All simulations were implemented using MATLAB.

Table 1. Parameters for OFDR sensing simulations.

Parameter	Symbol	Value
Wavelength sweep range	N/A	1549–1550 nm
Starting optical frequency	ν_0	193.414 THz
Ending optical frequency	ν_1	193.539 THz
Linewidth of the TL	$\Delta\lambda$ or $\Delta\nu$	8 fm or 1 MHz
Duration of a sweep	T	10 ms

2.1. Distance Sensing without Mode Hopping

To ensure the accuracy of simulation results, the mode-hopping-free simulation was first performed for OFDR distance sensing applications in free space. According to Table 1, the optical frequency sweep range of the TL is

$$\Delta F = \nu_1 - \nu_0 = 125 \text{ GHz}, \tag{1}$$

and the sweep rate can be calculated as follows:

$$k = \frac{\Delta F}{T} = 12.5 \text{ THz/s}. \tag{2}$$

Therefore, the two-point resolution of the OFDR system in free space can be expressed as [20]

$$\Delta z = \frac{c}{2n\Delta F} = 1.2 \text{ mm}, \tag{3}$$

where c is the speed of light in a vacuum and n is the refractive index of the medium (n = 1 in free space).

The instantaneous optical frequency of the reference arm's signal as a function of time t can be expressed as

$$\nu_{\mathrm{r}}(t) = kt + \nu_0. \tag{4}$$

The angular frequency of the sweeping signal in the reference arm is

$$\omega_{\mathrm{r}}(t) = 2\pi\nu_{\mathrm{r}}(t) = 2\pi(kt + \nu_0). \tag{5}$$

Thus, the phase of the signal can be described as

$$\varphi_{\mathrm{r}}(t) = \int \omega_{\mathrm{r}}(t)\,dt + e(t) = \pi k t^2 + 2\pi\nu_0 t + e(t), \tag{6}$$

where $e(t)$ is the phase noise induced by the TL's linewidth $\Delta\nu$ and can be expressed as a random walk Wiener process [21]:

$$e(t)_{t=kT_s} = \sum_{m=1}^{k} \varepsilon_m, \quad k = 1, 2, \ldots, \frac{T}{T_s}, \tag{7}$$

where T_s is the system's sampling interval and ε_m is a zero-mean Gaussian distributed random variable with a variance of $\sigma^2 = 2\pi\Delta\nu T_s$. Hence, the electric field of the reference arm's signal is

$$E_{\mathrm{r}}(t) = \exp[j\varphi_{\mathrm{r}}(t)] = \exp\left\{j\left[\pi k t^2 + 2\pi\nu_0 t + e(t)\right]\right\}. \tag{8}$$

Figure 2 illustrates the power spectral density of the simulated optical signal at 1550 nm, with a calculated linewidth of approximately 1 MHz. This result confirms the accuracy of the simulation parameters.

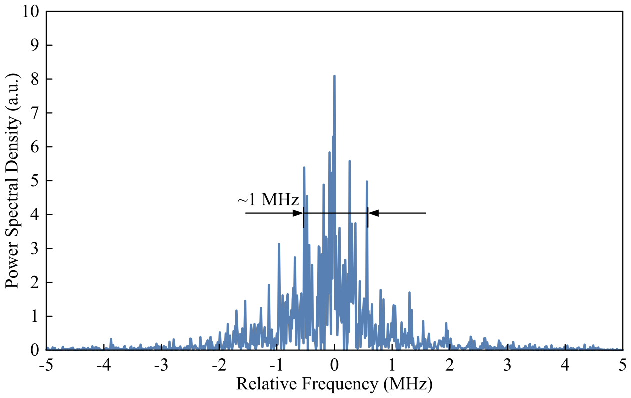

Figure 2. Power spectral density of the simulated 1550-nm optical signal.

As OFDR is a coherent homodyne technique, the TL's linewidth affects not only the signal noise but also the sensing distance of OFDR. Specifically, both the coherence length of the laser source and the system sampling rate determine the maximum sensing distance in free space. To achieve the maximum sensing distance limited by the TL and to avoid the impact of the sampling rate, the sampling rate was set high enough in all simulations. The coherence length can be calculated using the following equation:

$$L_c = \frac{\lambda^2}{n\Delta\lambda} \approx 300 \text{ m}, \tag{9}$$

where λ = 1549.5 nm represents the center wavelength and $\Delta\lambda$ = 8 fm is the linewidth. As a result, the maximum sensing distance of the OFDR system with a 1-MHz laser linewidth is half of the coherence length, or 150 m, in free space.

Assuming the distance between the DUT and the system is identical to the maximum sensing distance, the propagation delay can be denoted by

$$\tau = \frac{nL_c}{c} = 1 \text{ µs}. \tag{10}$$

Thus, the instantaneous optical frequency of the signal back reflected by the DUT as a function of time is

$$\nu_{\mathrm{d}}(t) = \nu_{\mathrm{r}}(t-\tau) = k(t-\tau) + \nu_0. \tag{11}$$

The frequency of the optical beat signal is a constant and expected to be

$$f_{\mathrm{beat}} = \nu_{\mathrm{r}}(t) - \nu_{\mathrm{d}}(t) = k\tau = 12.5 \text{ MHz}. \tag{12}$$

The beat frequency is proportional to the propagation delay and the distance between the DUT and the system. Figure 3 illustrates the instantaneous optical frequencies of the signals in both arms of the main interferometer. It is worth noting that the time delay τ has been magnified in the figure for improved visualization and does not represent its actual value.

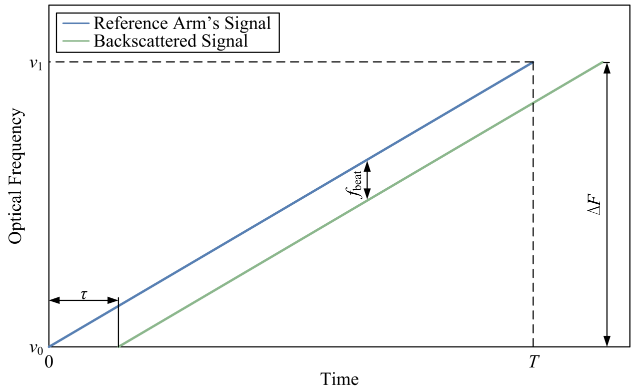

Figure 3. Instantaneous optical frequencies of signals without mode hopping in the main interferometer.

Similarly, the angular frequency of the backscattered sweeping signal is

$$\omega_{\mathrm{d}}(t) = \omega_{\mathrm{r}}(t-\tau) = 2\pi[k(t-\tau)+\nu_0], \tag{13}$$

and its phase can be expressed as

$$\varphi_{\mathrm{d}}(t) = \varphi_{\mathrm{r}}(t-\tau) = \pi k(t-\tau)^2 + 2\pi\nu_0(t-\tau) + e(t-\tau). \tag{14}$$

Therefore, the electric field of the backscattered signal is

$$E_{\mathrm{d}}(t) = R\exp\left\{j\left[\pi k(t-\tau)^2 + 2\pi\nu_0(t-\tau) + e(t-\tau)\right]\right\}, \tag{15}$$

where R is a randomly generated number centered around 1 with a 10% deviation representing reflectivity fluctuations.

When the reference arm's signal and the backscattered signal from the DUT interfere at the 50/50 optical coupler, the intensity of the optical beat signal acquired by the PD can be described as

$$I(t) = \|E_{\mathrm{r}}(t) + E_{\mathrm{d}}(t)\|^2. \tag{16}$$

To ensure clear observation of the time-domain signal, Figure 4a shows the 0.02-ms beat signal (4.99–5.01 ms) obtained from the simulation, with the DC component removed. The presence of interference fringes is distinctly discernible. Subsequently, a fast Fourier transform (FFT) is applied to the complete 10-ms dataset, resulting in the depiction of the optical beat signal in the spatial domain, as illustrated in Figure 4b.

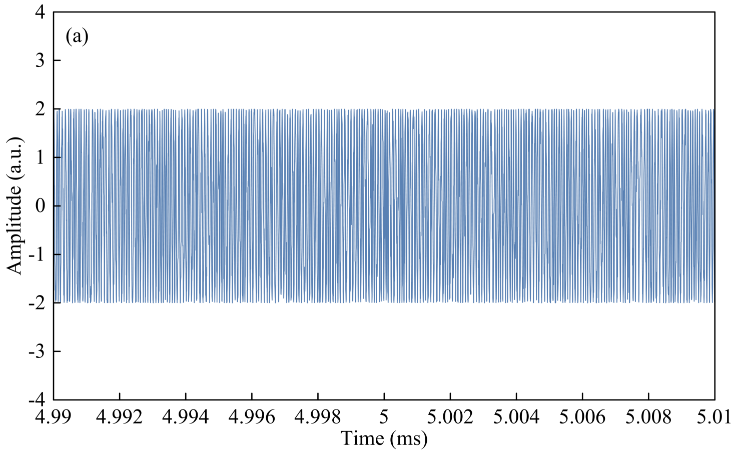

Figure 4. *Cont.*

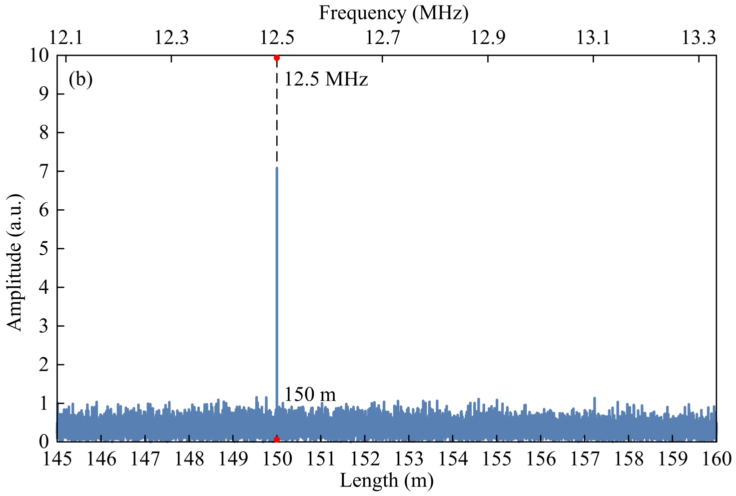

Figure 4. Optical beat signals without mode hopping in the 150-m DUT simulation. (**a**) The 0.02-ms data in the time domain. (**b**) The 10-ms complete data in the spatial domain.

Since OFDR LiDAR determines distances solely based on the location of the optical beat signal's peak in the spatial domain, the spatial resolution of the LiDAR system matches the 1.2-mm two-point resolution. In Figure 4b, the interference signal was measured to have a frequency of 12.5 MHz, enabling us to determine the distance between the DUT and the system to be 150 m. These results obtained from the mode-hopping-free simulation align with the theoretical assumptions and analysis, providing evidence of the rationality and effectiveness of the simulation and serving as a foundation for further simulations incorporating mode hopping.

2.2. *Distance Sensing with Mode Hopping*

In this simulation, the optical frequency tuning of the TL experienced mode hopping, which was induced by assuming that it occurred at T_h = 5 ms. This resulted in an optical frequency jump ν_h of 12.5 GHz (0.1 nm). All other parameters were held constant. Hence, the instantaneous optical frequency of the reference arm's signal becomes

$$\nu_\mathrm{r}(t) = \begin{cases} kt + \nu_0, & \text{if } t \leq T_\mathrm{h} \\ kt + \nu_0 + \nu_\mathrm{h}, & \text{if } t > T_\mathrm{h} \end{cases}. \tag{17}$$

The electric field of the signal is

$$E_\mathrm{r}(t) = \begin{cases} \exp\{j[\pi k t^2 + 2\pi\nu_0 t + e(t)]\}, & \text{if } t \leq T_\mathrm{h} \\ \exp\{j[\pi k t^2 + 2\pi(\nu_0 + \nu_\mathrm{h})t + e(t)]\}, & \text{if } t > T_\mathrm{h} \end{cases}. \tag{18}$$

The propagation delay τ does not change for the same DUT, so the instantaneous optical frequency of the backscattered signal is

$$\nu_\mathrm{d}(t) = \begin{cases} k(t-\tau) + \nu_0, & \text{if } t \leq T_\mathrm{h} + \tau \\ k(t-\tau) + \nu_0 + \nu_\mathrm{h}, & \text{if } t > T_\mathrm{h} + \tau \end{cases}. \tag{19}$$

Figure 5 presents the optical frequencies of the signals with mode hopping in both arms. For the purpose of enhanced visualization, the propagation delay was also magnified in the figure.

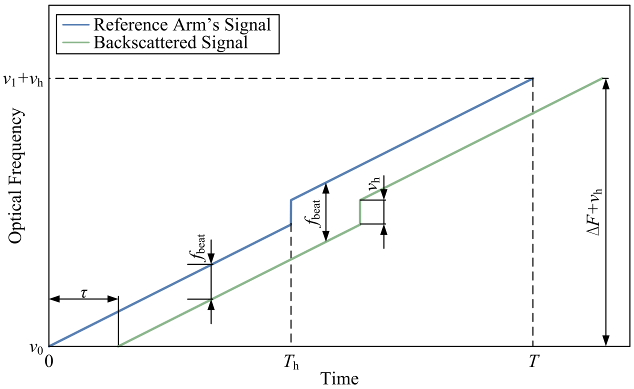

Figure 5. Instantaneous optical frequencies of signals with mode hopping in the main interferometer.

Due to mode hopping, the frequency of the beat signal is no longer constant over a complete optical frequency sweep. The beat frequency as a function of time can be described as

$$f_{\text{beat}}(t) = \begin{cases} k\tau = 12.5\ \text{MHz}, & \text{if } t \le T_{\text{h}} \cup t > T_{\text{h}} + \tau \\ k\tau + \nu_{\text{h}} = 12.5125\ \text{GHz}, & \text{if } T_{\text{h}} < t \le T_{\text{h}} + \tau \end{cases}. \tag{20}$$

The beat frequencies of 12.5 MHz and 12.5125 GHz correspond to distances of 150 m and 150.15 km in free space, respectively. This implies that two individual peaks exist in the spectrum of the beat signal in the spatial domain. However, the peak at 150.15 km is an incorrect distance measurement caused by mode hopping and does not correspond to the presence of a DUT at that position in the simulation. This peak could affect the accuracy of determining the distance between the DUT and the system.

According to Equation (18), the electric field of the backscattered signal can be expressed as

$$E_{\text{d}}(t) = \begin{cases} R\exp\{j[\pi k(t-\tau)^2 + 2\pi\nu_0(t-\tau) + e(t-\tau)]\}, & \text{if } t \le T_{\text{h}} + \tau \\ R\exp\{j[\pi k(t-\tau)^2 + 2\pi(\nu_0+\nu_{\text{h}})(t-\tau) + e(t-\tau)]\}, & \text{if } t > T_{\text{h}} + \tau \end{cases}. \tag{21}$$

Similarly, the intensity of the optical beat signal can be calculated using Equation (16) when the reference arm's signal and the backscattered signal interfere at the 50/50 optical coupler. To enhance observation, Figure 6a presents a 0.02-ms optical beat signal (4.99–5.01 ms) in the time domain using a DC blocking filter in the simulation. Notably, a distinct high-frequency beat signal emerges, starting from 5 ms and lasting for 1 µs, which is attributed to mode hopping.

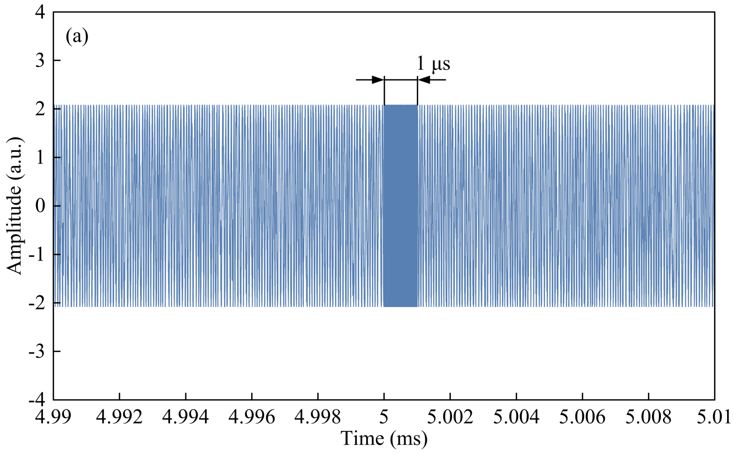

Figure 6. *Cont.*

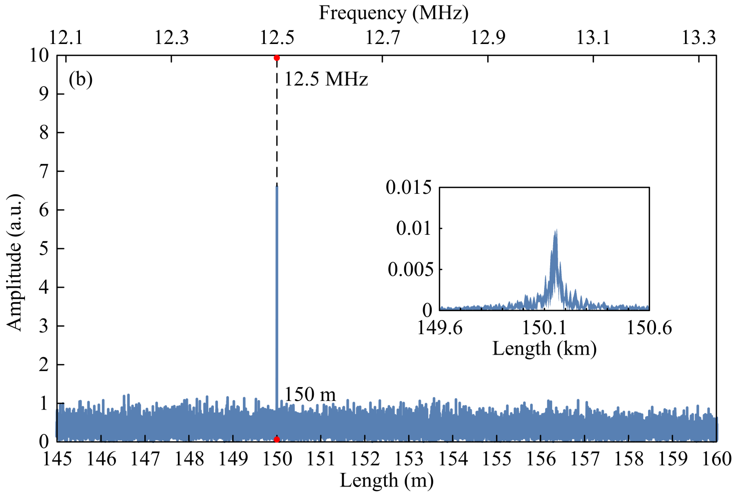

Figure 6. Optical beat signals with mode hopping in the 150-m DUT simulation. (**a**) The 0.02-ms data in the time domain. (**b**) The 10-ms complete data in the spatial domain.

Furthermore, Figure 6b illustrates the spatial-domain beat signal obtained by performing an FFT on a complete data cycle. In this case, the 1.2-mm spatial resolution remains unchanged as the nominal wavelength sweep range does not vary, and the peak at 150 m remains visible. Additionally, a false peak at 150.15 km, caused by mode hopping, is also observable as shown in the inset. However, the duration of the high-frequency beat signal generated by mode hopping plays an important role in affecting OFDR performance. Due to the limited duration of the 12.5125-GHz beat signal (τ or 1 µs), which occupies merely 0.01% of a 10-ms sweep cycle, the intensity of this mode hopping-induced peak is significantly smaller. Therefore, the presence of a peak at an incorrect position, resulting from mode hopping, has minimal impact and does not mislead the judgment of the DUT's actual distance.

The 1-µs propagation delay represents the longest delay within the coherence length of the DFB laser source. Any DUT located closer than 150 m from the system would incur a shorter propagation delay and exhibit a weaker peak intensity at the incorrect position, which would not affect the accuracy of determining the distance to the DUT.

Moreover, in practical implementation, an OFDR LiDAR distance sensing system with an MHz-level sampling rate and constrained computational and storage resources would face challenges in detecting a peak at a distance of hundreds of kilometers. To prevent spectrum aliasing and preserve the integrity of the signal, a low-pass electrical filter can be used before signal digitization to filter out frequencies higher than the Nyquist frequency. Consequently, the false peak caused by mode hopping does not influence the distance sensing of the actual DUT. Therefore, it can be concluded that mode hopping does not hinder the performance of the OFDR distance sensing system, which employs a low-cost DFB laser with a linewidth of 1 MHz and a wavelength sweep range of 1 nm.

3. Distributed Strain Sensing Simulations

Based on the results of the OFDR LiDAR sensing simulations, additional simulations were conducted to assess the performance of the OFDR distributed strain sensing system shown in Figure 7. This system shares many components and devices with the LiDAR system presented in Section 2. Instead, the second port of the optical circulator is connected to the fiber under test (FUT). The central segment of the FUT is positioned between two translation stages for the purpose of distributed strain sensing. A Vernier micrometer with 1-µm sensitivity operates in one of the stages, thereby inducing strain on the sensing fiber.

In the strain sensing simulations, all parameters remained constant except for the refractive index n, which was adjusted to 1.5 to account for the transition from free space to fused silica glass as the light propagation medium. The TL's two-point resolution and coherence length were recalculated using Equations (3) and (9), respectively. The resulting two-point resolution was found to be Δz = 0.8 mm, while the coherence length of the TL was determined as $L_c \approx 200$ m.

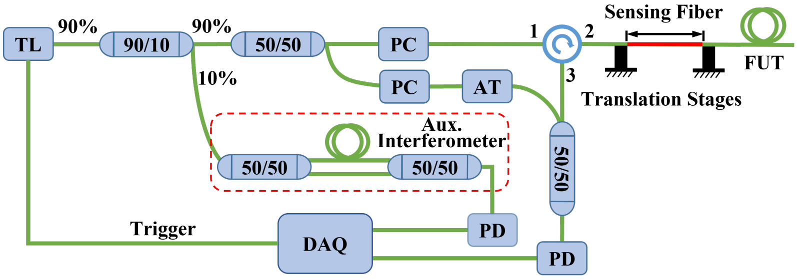

Figure 7. Schematic of an OFDR distributed strain sensing system.

3.1. Strain Sensing without Mode Hopping

To emulate a FUT in the simulation, the fiber was divided into a series of discrete points. The spacing between adjacent fiber points was set to match the two-point resolution of the system (0.8 mm) to prevent missing frequencies or frequency mismatches in the spatial domain. The simulation considered a 100-m FUT, which is half of the coherence length of the TL. The FUT comprised a total of 125,000 fiber points, referred to as N. In addition, 100 µε was uniformly applied on the FUT from the 5-m position to the 95-m position. Figure 8 displays the FUT before and after applying the strain.

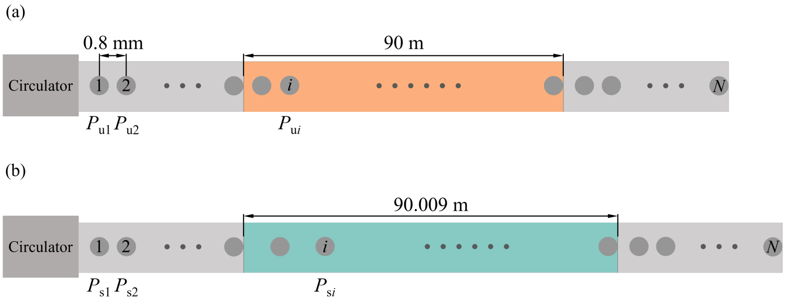

Figure 8. The 100-m FUT comprising discrete fiber points. (**a**) No strain applied. (**b**) Application of 100 µε from the 5-m position to the 95-m position.

As shown in Figure 8, P_{ui} denotes the position of the i-th fiber point (i = 1, 2, 3, . . . , N) in the unstrained case, while P_{si} denotes the position of the same fiber point with strain applied. P_{ui} can be expressed as

$$P_{ui} = i\Delta z. \tag{22}$$

In the unstrained case, the propagation delay caused by the i-th fiber point, denoted as τ_i, can be calculated using Equation (10). The electric field of the backscattered signal from this point can then be obtained as follows:

$$E_i(t) = R\exp\left\{j\left[\pi k(t-\tau_i)^2 + 2\pi\nu_0(t-\tau_i) + e(t-\tau_i)\right]\right\}. \tag{23}$$

The electric field of the reference arm's signal, denoted as $E_r(t)$, can be obtained through Equation (8). The intensity of the optical beat signal contributed by the i-th fiber point can then be calculated as follows:

$$I_i(t) = \|E_r(t) + E_i(t)\|^2. \tag{24}$$

Thus, the Rayleigh backscattering fingerprint of the i-th fiber point in the unstrained case can be obtained, which resembles the pattern shown in Figure 4. Since the FUT is considered a superposition of all its discrete fiber points, the intensity of the interference signal generated by the reference arm and the entire FUT can be expressed as

$$I(t) = \sum_{i=1}^{N} I_i(t). \tag{25}$$

As shown in Figure 8b, the application of strain on the central 90-m section of the FUT results in a uniform increase in the distance between adjacent fiber points in this section. The new position of the i-th fiber point under strain can be represented as

$$P_{si} = \begin{cases} i\Delta z, & P_{ui} \leq P_l \\ i\Delta z + S(P_{ui} - P_l), & P_l < P_{ui} \leq P_r, \\ i\Delta z + SL_s, & P_{ui} > P_r \end{cases} \tag{26}$$

where S = 100 με represents the strain applied to the central fiber section. P_l = 5 m and P_r = 95 m denote the initial positions of the left and right ends of the fiber section before it was stretched, respectively. L_s is the original length of the central fiber segment, equal to the difference between P_l and P_r (90 m).

In addition to changes in the positions of fiber points, the application of strain in the central fiber section also causes a reduction in its refractive index due to the elasto-optic effect [22]. However, the increase in the physical length of the fiber dominates and leads to an increase in the optical path length when tensile strain is applied. Specifically, the refractive index of the fiber was decreased by $\Delta n = 3 \times 10^{-5}$ under a strain of 100 με [23,24], while the refractive index remained constant (n = 1.5) across the other unstrained sections of the fiber.

When both the positions of fiber points and the refractive index are subject to change due to strain, Equation (10) cannot be used directly to calculate the propagation delay for each fiber point in the strained case. Instead, the propagation delay for the i-th fiber point in the strained case depends on the original position of the point and can be expressed as follows:

$$\tau_{si} = \begin{cases} \frac{2nP_{si}}{c}, & P_{ui} \leq P_l \\ \frac{2nP_l + 2(n-\Delta n)(P_{si} - P_l)}{c}, & P_l < P_{ui} \leq P_r. \\ \frac{2(n-\Delta n)(1+S)L_s + 2n(P_l + P_{ui} - P_r)}{c}, & P_{ui} > P_r \end{cases} \tag{27}$$

Consequently, the intensity of the interference signal generated by the reference arm and the entire FUT in the strained case can be calculated using Equation (23) through (25) in conjunction with the propagation delay described above. FFTs were performed on the signals collected by the PD in both unstrained and strained cases to obtain mode-hopping-free optical beat signals in the spatial domain. The Rayleigh backscattering profiles of the FUT are shown in Figure 9.

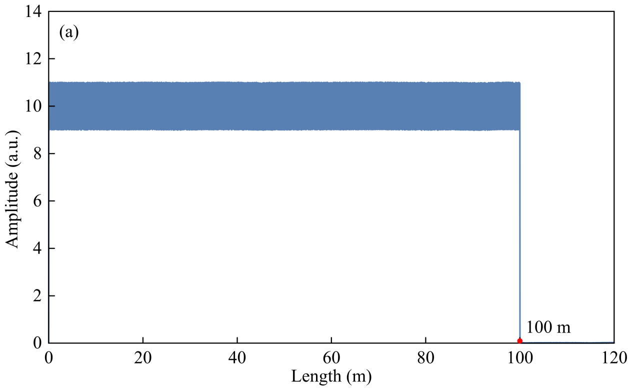

Figure 9. *Cont.*

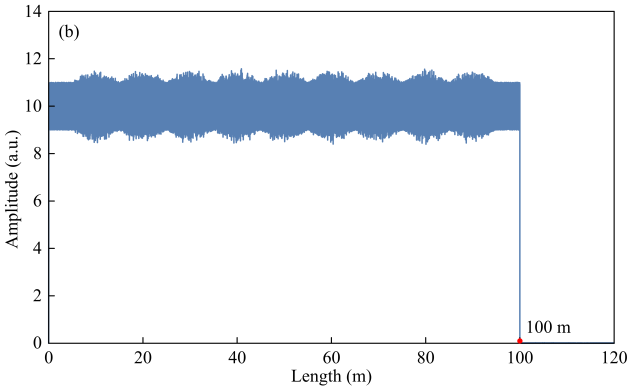

Figure 9. Spatial-domain optical beat signals without mode hopping under different strain conditions. (**a**) No strain applied. (**b**) Application of 100 με to the central 90-m section.

The unstrained data shown in Figure 9a were used as the reference spectrum, while the strained data shown in Figure 9b were treated as the measurement spectrum. Both spectra contained 125,000 data points ranging from 0 to 100 m in the spatial domain. Considering the heavy computational load, the spectra were segmented into 2500 equally sized windows, each comprising 50 data points. These windows were connected end-to-end in the simulation. Based on the product of the number of data points in each window and the 0.8-mm two-point resolution, the sensing resolution of the strain sensing system was calculated to be 40 mm, which meets the requirements of most practical projects using the 1-nm OFDR interrogator.

Two windows with identical spatial position indices were extracted from the reference and measurement spectra, respectively. These windows were zero-padded and then transformed from the spatial domain back to the optical frequency domain using inverse FFTs. This process facilitated the calculation of the corresponding Rayleigh backscattering spectrum (RBS) for each window. Figure 10 illustrates the RBS of the first window from the central 90-m FUT under both unstrained and strained conditions.

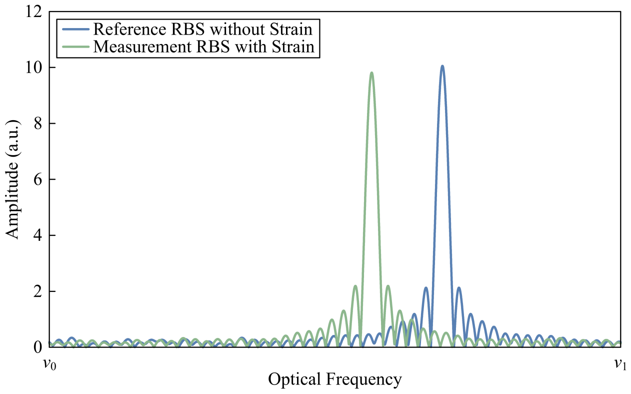

Figure 10. Optical frequency-domain RBS without mode hopping under different strain conditions.

The application of strain in the central fiber section caused a shift in the RBS in the optical frequency domain. To determine the extent of this shift, cross-correlation can be utilized on the two RBS in the unstrained and strained cases. The resulting shift is proportional to the strain change at the current window, and this process would be repeated for all windows to obtain the complete strain distribution throughout the FUT. Figure 11 shows the strain measurement results of the distributed strain sensing simulation for the entire 100-m FUT.

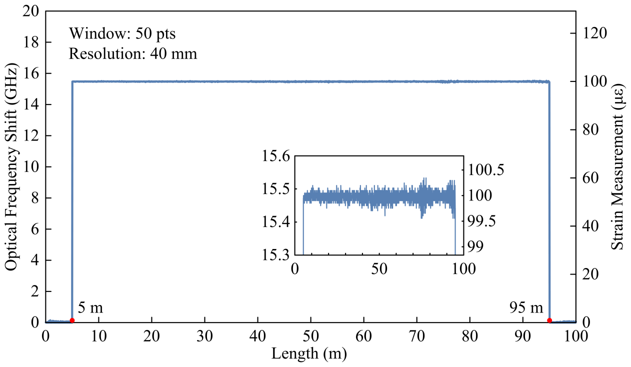

Figure 11. Measurement results of mode-hopping-free distributed strain sensing simulation for a 100-m FUT with 100 με applied.

In the above figure, an optical frequency shift of approximately 16 GHz is observed along the central 90-m fiber section where 100 με was applied. In contrast, no significant optical frequency shift is detected in the remaining sections of the FUT, indicating the absence of strain in those fiber segments. This outcome aligns with the parameters and settings utilized in the simulation.

Upon closer inspection of the inset, slight variations in strain measurements are discernible in the central fiber section, resulting from random errors. Nevertheless, the average strain sensitivity coefficient, calculated as the mean ratio of the optical frequency shift to the applied strain, amounts to 0.1548 GHz/με, which closely matches the reported value of 0.15 GHz/με [25]. Moreover, the strain measurement results for the central fiber segment remain within 15.48 ± 0.07 GHz or 100 ± 0.45 με, with the standard deviation being less than 0.015 GHz or 0.1 με for the entire 90-m segment and 0.017 GHz or 0.11 με for the second half of the segment. These findings confirm that the simulation results are remarkably reliable.

3.2. Strain Sensing with Mode Hopping

To delve deeper into the impact of mode hopping on distributed strain sensing, an optical frequency jump was also introduced into the sweep, as depicted in Figure 5, with T_h set to a random value between 0 and T. In this simulation, all other parameters remained consistent with those employed in the mode-hopping-free strain sensing simulation. The electric field of the reference arm's signal mirrored that of the distance sensing simulation with mode hopping, as specified by Equation (18).

In the unstrained case, the position and propagation delay of the i-th fiber point on the FUT can be calculated using Equations (22) and (10), respectively. The electric field of the signal backscattered by the i-th fiber point is given by

$$E_i(t) = \begin{cases} R\exp\{j[\pi k(t-\tau_i)^2 + 2\pi\nu_0(t-\tau_i) + e(t-\tau_i)]\}, & \text{if } t \leq T_\mathrm{h} + \tau_i \\ R\exp\{j[\pi k(t-\tau_i)^2 + 2\pi(\nu_0+\nu_\mathrm{h})(t-\tau_i) + e(t-\tau_i)]\}, & \text{if } t > T_\mathrm{h} + \tau_i \end{cases}. \tag{28}$$

Similarly, the application of strain on the FUT affected various optical properties, including the position of the fiber point, the refractive index, and the propagation delay. These properties can be calculated using Equations (26) and (27). Furthermore, the electric field of the backscattered signal can be determined using Equation (28), taking into consideration the propagation delay in the strained case.

The intensity of the interference signal produced by the reference arm and the entire FUT can be acquired using Equations (24) and (25) in both unstrained and strained cases. The beat signals in the spatial domain before and after the strain was applied within the 100-m FUT, which can be obtained by performing FFTs on the optical frequency-domain signals collected by the PD, are shown in Figure 12.

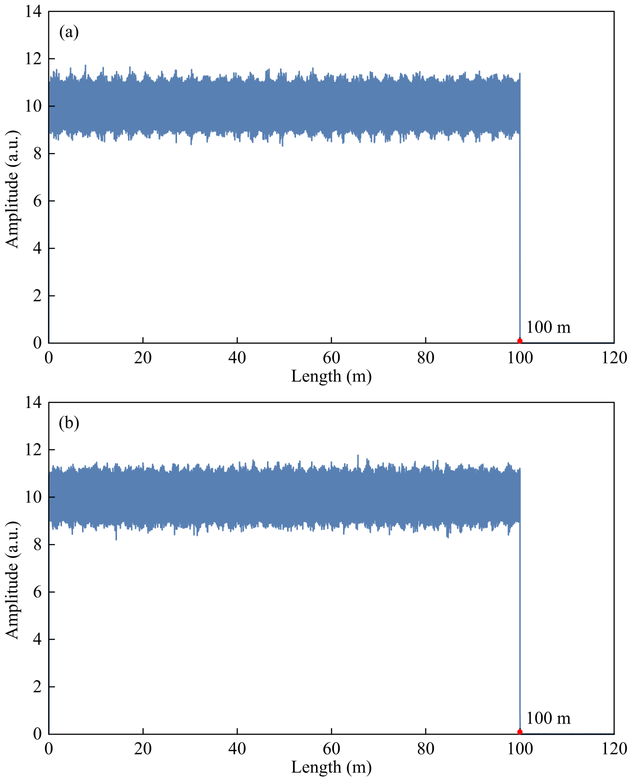

Figure 12. Spatial-domain optical beat signals with mode hopping under different strain conditions. (**a**) No strain applied. (**b**) Application of 100 με to the central 90-m section.

The RBS of the first window on the central 90-m FUT is illustrated in Figure 13 for both unstrained and strained conditions. The resulting shift induced by strain in the optical frequency domain is clearly observable below.

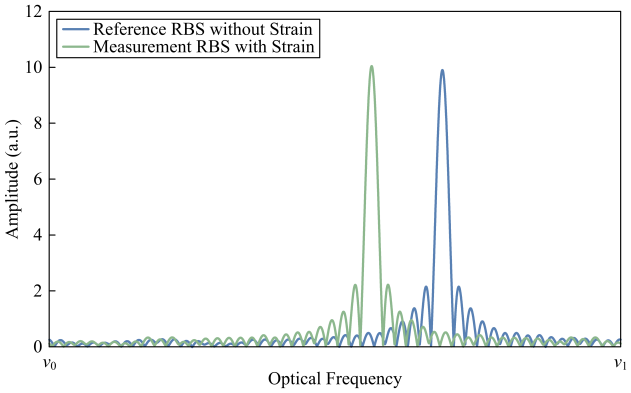

Figure 13. Optical frequency-domain RBS with mode hopping under different strain conditions.

To perform distributed strain sensing, cross-correlation was applied to all windows along the 100-m FUT. The strain measurement results are depicted in Figure 14.

In comparison to Figure 11, Figure 14 presents a similar optical frequency shift of around 16 GHz spanning from 5 m to 95 m in the spatial domain. As illustrated in the inset, however, the optical frequency shift experiences increased fluctuations along the FUT due to the presence of mode hopping. These fluctuations intensify towards the end of the FUT, indicating a growing impact of mode hopping with greater distance and propagation delay. Nevertheless, the results of the distributed strain sensing simulation remain satisfactory.

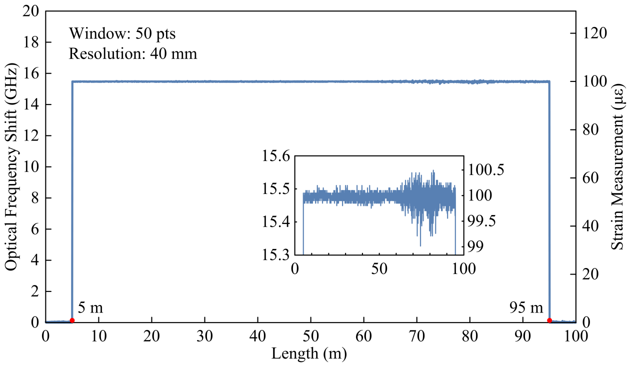

Figure 14. Measurement results of distributed strain sensing simulation with mode hopping for a 100-m FUT with 100 με applied.

The average strain sensitivity coefficient is calculated to be 0.1547 GHz/με, which is still reasonably close to the reference value of 0.15 GHz/με. In the central 90-m fiber segment, the strain measurement results are within 15.47 ± 0.15 GHz or 100 ± 0.97 με, while the standard deviation is less than 0.02 GHz or 0.13 με for the entire 90-m segment and 0.026 GHz or 0.17 με for the second half of the segment. Although these values represent a two-fold increase compared to their counterparts in the mode-hopping-free scenario, they remain highly acceptable with measurement errors under 1% and meet the requirements for most practical OFDR distributed monitoring applications.

The results signify that mode hopping does not significantly affect the performance of the low-cost OFDR distributed strain sensing system that employs a 1-nm DFB laser source. Moreover, post-processing methods such as image processing and averaging [26–29] can be utilized to suppress glitches and further alleviate the impacts of mode hopping on the distributed strain sensing performance of OFDR.

4. Conclusions and Discussion

This article investigates the influences of mode hopping in telecom DFB lasers on the performance of OFDR-based LiDAR and distributed strain sensing applications. Through numerical analysis and simulations, it is suggested that misjudgments in distance sensing caused by mode hopping are highly negligible due to the short propagation delay and low sampling rate. Furthermore, only a minimal impact on distributed strain sensing, with a fluctuation range less than 1% of the induced strain, is observed within the coherence length of the tunable laser source. This confirms the dependable sensing performance of OFDR systems. This study demonstrates the potential of developing and expanding OFDR sensing interrogators employing low-cost telecom DFB lasers in practice. Further research could explore the impacts of multiple mode hops through simulations and experimental verification, as well as approaches to diminish the effects of mode hopping and enhance the effectiveness of economical OFDR sensing interrogation systems.

Author Contributions: Conceptualization, Q.W. and K.P.C.; methodology, Q.W.; validation, Q.W., N.L., K.Z., S.Z., G.Z. and K.P.C.; writing—original draft preparation, Q.W.; writing—review and editing, Q.W., N.L., K.Z., S.Z., G.Z., R.W. and K.P.C.; visualization, Q.W.; supervision, K.P.C.; project administration, R.W. and K.P.C.; funding acquisition, R.W. and K.P.C. All authors have read and agreed to the published version of the manuscript.

Funding: This research was funded by the Department of Energy through Grant DE-FE00032210 and Grant DE-NE0009402. This work was also supported by the Department of Energy, National Energy Technology Laboratory, an agency of the United States Government, through a support contract with Leidos Research Support Team (LRST).

Institutional Review Board Statement: Not applicable.

Informed Consent Statement: Not applicable.

Data Availability Statement: Data underlying the results presented in this paper are not publicly available at this time but may be obtained from the authors upon reasonable request.

Conflicts of Interest: The authors declare no conflicts of interest.

References

1. Ohanian, O.J.; Yakusheva, A.A.; Kreger, S.T.; Kominsky, D.; Soller, B.J.; Tran, M.; Komljenovic, T.; Bowers, J.E. OFDR on photonic circuits: Fiber optic sensing infrastructure and applications. In Proceedings of the 26th International Conference on Optical Fiber Sensors, Lausanne, Switzerland, 24–28 September 2018.
2. Badar, M.; Lu, P.; Wang, Q.; Boyer, T.; Chen, K.P.; Ohodnicki, P. Real-time optical fiber-based distributed temperature monitoring of insulation oil-immersed commercial distribution power transformer. *IEEE Sens. J.* **2021**, *21*, 3013–3019. [CrossRef]
3. Lalam, N.; Lu, P.; Lu, F.; Hong, T.; Badar, M.; Buric, M. Distributed carbon dioxide sensor based on sol-gel silica-coated fiber and optical frequency domain reflectometry (OFDR). In *ODS 2020: Industrial Optical Devices and Systems*; SPIE: Bellingham, WA, USA, 2020.
4. Badar, M.; Lu, P.; Wang, Q.; Boyer, T.; Chen, K.P.; Ohodnicki, P. Monitoring internal power transformer temperature using distributed optical fiber sensors. In *Optical Waveguide and Laser Sensors*; SPIE: Bellingham, WA, USA, 2020.
5. Iida, D.; Honda, N.; Oshida, H. Advances in distributed vibration sensing for optical communication fiber state visualization. *Opt. Fiber Technol.* **2020**, *57*, 102263. [CrossRef]
6. Barrias, A.; Casas, J.R.; Villalba, S. Fatigue performance of distributed optical fiber sensors in reinforced concrete elements. *Constr. Build. Mater.* **2019**, *218*, 214–223. [CrossRef]
7. Liu, Q.; Fan, X.; He, Z. Time-gated digital optical frequency domain reflectometry with 1.6-m spatial resolution over entire 110-km range. *Opt. Express* **2015**, *23*, 25988–25995. [CrossRef] [PubMed]
8. Wu, Y.; Deng, L.; Yang, K.; Liang, W. Narrow linewidth external cavity laser capable of high repetition frequency tuning for FMCW LiDAR. *IEEE Photonics Technol. Lett.* **2022**, *34*, 1123–1126. [CrossRef]
9. Huang, S.; Zhu, T.; Yin, G.; Lan, T.; Li, F.; Huang, L.; Liu, M. Dual-cavity feedback assisted DFB narrow linewidth laser. *Sci. Rep.* **2017**, *7*, 1185. [CrossRef] [PubMed]
10. Virtanen, H.; Uusitalo, T.; Karjalainen, M.; Ranta, S.; Viheriälä, J.; Dumitrescu, M. Narrow-linewidth 780-nm DFB lasers fabricated using nanoimprint lithography. *IEEE Photonics Technol. Lett.* **2018**, *30*, 51–54. [CrossRef]
11. Wang Z.; Jeon, I.; Ahn, C.; Kim, J. Narrow linewidth, arbitrarily tuning DFB laser using 3 × 3 optical coupler-based fully digital feedback. *J. Light. Technol.* **2024**, *42*, 3820–3825. [CrossRef]
12. Wang, Q.; Zhao, K.; Badar, M.; Lu, P.; Zhao, J.; Li, Y.; Chen, K.P. Low-cost OFDR distributed fiber sensing enabled by fiber with enhanced Rayleigh backscattering. In Proceedings of the Conference on Lasers and Electro-Optics (CLEO), San Jose, CA, USA, 9–14 May 2021.
13. Chinone, N.; Kuroda, T.; Ohtoshi, T.; Takahashi, T.; Kajimura, T. Mode-hopping noise in index-guided semiconductor lasers and its reduction by saturable absorbers. *IEEE J. Quantum Electron.* **1985**, *21*, 1264–1270. [CrossRef]
14. Heumier, T.A. Mode Hopping in Semiconductor Lasers. Ph.D. Dissertation, Montana State University, Bozeman, MT, USA, 1992.
15. Zhang, Y.; Yang, F.; Liu, G.; Li, G.; Xiang, M.; Lu, Q.; Donegan, J.F.; Guo, W. Experimental demonstration of an easy-to-fabricate 1.3-µm directly modulated DFB laser with improved beam profile. *J. Light. Technol.* **2023**, *41*, 3094–3101. [CrossRef]
16. Kasai, K.; Nakazawa, M.; Tomomatsu, Y.; Endo, T. 1.5 µm, mode-hop-free full C-band wavelength tunable laser diode with a linewidth of 8 kHz and a RIN of −130 dB/Hz and its extension to the L-band. *Opt. Express* **2017**, *25*, 22113–22124. [CrossRef] [PubMed]
17. Zhao, Y.; Shi, Y.; Li, J.; Liu, S.; Xiao, R.; Li, L.; Lu, J.; Chen, X. A cascaded tunable DFB semiconductor laser with compact structure. *IEEE J. Quantum Electron.* **2018**, *54*, 2200111. [CrossRef]
18. Pintus, P.; Guo, J.; Tran, M.A.; Jin, W.; Liang, J.; Peters, J.; Xiang, C.; Ohanian, O.J.; Bowers, J.E. Demonstration of large mode-hop-free tuning in narrow-linewidth heterogeneous integrated laser. *J. Light. Technol.* **2023**, *41*, 6723–6734. [CrossRef]
19. Badar, M.; Lu, P.; Wang, M.; Wang, Q.; Chen, K.P.; Buric, M.; Ohodnicki, P. Integrated auxiliary interferometer to correct non-linear tuning errors in OFDR. In *Optical Waveguide and Laser Sensors*; SPIE: Bellingham, WA, USA, 2020.
20. Wang, Q.; Zhao, K.; Badar, M.; Yi, X.; Lu, P.; Buric, M.; Mao, Z.H.; Chen, K.P. Improving OFDR distributed fiber sensing by fibers with enhanced Rayleigh backscattering and image processing. *IEEE Sens. J.* **2022**, *22*, 18471–18478. [CrossRef]
21. Zhou, X.; Gao, Y.; Huo, J.; Shieh, W. Theoretical analysis of phase noise induced by laser linewidth and mismatch length in self-homodyne coherent systems. *J. Light. Technol.* **2021**, *39*, 1312–1321. [CrossRef]
22. Kiiveri, P.; Kuusisto, M.; Koponen, J.; Kimmelma, O.; Aallos, V.; Harra, J.; Husu, H.; Kyllönen, P. Refractive index profiles and propagation losses in bent optical fibers. *Opt. Eng.* **2022**, *61*, 126106. [CrossRef]
23. Hill, K.O.; Meltz, G. Fiber Bragg grating technology fundamentals and overview. *J. Light. Technol.* **1997**, *15*, 1263–1276. [CrossRef]
24. Rao, Y. In-fibre Bragg grating sensors. *Meas. Sci. Technol.* **1997**, *8*, 355–375. [CrossRef]
25. *OBR 4600 Optical Backscatter Reflectometer, OBR 4600 Datasheet*; Luna Innovations: Blacksburg, VA, USA, 2019.
26. Soto, M.A.; Ramírez, J.A.; Thévenaz, L. Reaching millikelvin resolution in Raman distributed temperature sensing using image processing. In *Sixth European Workshop on Optical Fibre Sensors*; SPIE: Bellingham, WA, USA, 2016.
27. Zhao, S.; Cui, J.; Wu, Z.; Tan, J. Accuracy improvement in OFDR-based distributed sensing system by image processing. *Opt. Lasers Eng.* **2020**, *124*, 105824. [CrossRef]

28. Wang, Q.; Zhao, K.; Yi, X.; Zhao, J.; Zhong, S.; Chen, K.P. Low-cost OFDR distributed sensing based on optical fiber with enhanced Rayleigh backscattering profiles and median filtering. In Proceedings of the 27th International Conference on Optical Fiber Sensors, Alexandria, VA, USA, 29 August–2 September 2022.
29. Soto, M.A.; Yang, Z.; Ramírez, J.A.; Zaslawski, S.; Thévenaz, L. Evaluating measurement uncertainty in Brillouin distributed optical fibre sensors using image denoising. *Nat. Commun.* **2021**, *12*, 4901. [CrossRef] [PubMed]